J. Nanostruct Chem. 2026; 16(5): 428-442

Journal of Nanostructure in Chemistry (JNSC)

https://doi.org/10.57647/jnsc.2026.1605.22

Research Article

Surface Modification of Cardiovascular Stents with TiO_2 Nanotube Arrays: In Vitro Investigation of Interfacial Properties and Endothelialization

Changcun Fang, Lei Chen, Fei Liu*

Postdoctoral Scientific Research Workstation, Engineering Research Center for Sugar and Sugar Complex, National-Local Joint Engineering Laboratory of Polysaccharide Drugs, Key Laboratory of Carbohydrate and Glycoconjugate Drugs, Shandong Academy of Pharmaceutical Science, Jinan, Shandong 250101, China

* **Corresponding authors:** liufei@sdaps.cn

Article History:

Received:
12 March 2026

Revised:
14 April 2026

Accepted:
04 May 2026

Published in Issue:
31 October 2026

Abstract

The long-term performance of cardiovascular stents is compromised by pathological events such as restenosis and late thrombotic failure, which together motivate surface-engineering strategies that can promote vascular healing while regulating the earliest interfacial events. In this study, titanium dioxide (TiO_2) nanotube (TNT) arrays were fabricated on Ti-6Al-4V alloy by electrochemical anodization and subsequently annealed at 450 °C and 600 °C to tune their crystalline phase. FESEM, TEM, XRD, Raman spectroscopy, XPS, AFM, and water-contact-angle analysis were used to characterize the resulting morphological, structural, and chemical changes. The data show that the interfacial behavior of the nanotube layers is strongly phase dependent. Among the tested surfaces, the 450 °C-annealed TNTs, characterized by an anatase-rich structure and a superhydrophilic response, displayed the most favorable albumin-over-fibrinogen adsorption pattern and supported the strongest HUVEC attachment and proliferation. These results indicate that moderate annealing yields an interfacial environment in which ordered nanotopography, anatase-dominated crystallinity, and hydration-favorable surface chemistry act together to support endothelialization. Compared with both the amorphous TNT-As layer and the more strongly transformed TNT-600 surface, TNT-450 appears to occupy a more favorable physicochemical window in which surface hydration, adsorption selectivity, and cell-facing interactions are balanced most effectively. The mixed-phase TNT-600 surface still performed better than the bare alloy, but its partially rutile-containing interface showed a weaker combination of wettability, protein selectivity, and endothelial response than TNT-450, indicating that excessive thermal transformation is not advantageous under the present conditions. Overall, phase-engineered TiO_2 nanotube arrays represent a promising drug-free strategy for improving stent-surface biointegration. Direct dynamic blood-contact validation under flow and stent-form conditions remains an important next step.

Keywords: Biointegration; Cardiovascular stent; Electrochemical anodization; Endothelialization; Interfacial protein adsorption; Surface modification; TiO_2 nanotubes

Cite this article: Fang Ch., Chen L., Liu F.Surface Modification of Cardiovascular Stents with TiO_2 Nanotube Arrays: In Vitro Investigation of Interfacial Properties and Endothelialization. *J Nanostruct Chem* **16**, 428-442 (2026).
https://doi.org/10.57647/jnsc.2026.1605.22

1. Introduction

Coronary artery disease (CAD) remains a leading cause of morbidity and mortality worldwide, with percutaneous coronary intervention (PCI) and stenting being the primary revascularization strategies. The evolution of stent technology has progressed from bare-metal stents (BMS) to drug-eluting stents (DES), each designed to address specific clinical challenges [1]. Although bare-metal stents (BMS) successfully mitigate acute vascular collapse, their therapeutic window is constrained by prevalent in-stent restenosis (ISR), a pathological process characterized by the exuberant proliferation of vascular smooth muscle cells (SMCs) alongside neointimal hyperplasia [2]. While the advent of drug-eluting stents (DES), which release antiproliferative drugs, significantly curtailed ISR rates, their clinical utility is frequently offset by compromised vascular repair, deficient re-endothelialization, and an elevated vulnerability to late stent thrombosis (LST), a life-threatening sequela that necessitates prolonged dual antiplatelet therapy [3-4]. Furthermore, the polymer matrices integrated into numerous DES designs can trigger persistent inflammatory cascades, which further impede vascular healing [5]. Such drawbacks have catalyzed rigorous exploration into innovative methodologies capable of concurrently suppressing SMC hyperplasia and accelerating the establishment of a physiologically functional endothelial layer, representing an endogenous, non-thrombogenic surface [6-7].

Surface functionalization of the metallic stent substrate provides a drug-free route to improve vascular healing by regulating the earliest events at the biomaterial-liquid interface while also supporting endothelial recovery. Titanium and Ti-6Al-4V remain attractive model substrates because of their corrosion resistance, mechanical robustness, and broad biomedical use [8-9]. Importantly, nanoscale modification of titanium can alter water structuring, surface energy, protein adsorption, and endothelial cell attachment, thereby changing the biological fate of the implant [10-11]. Among the available strategies, self-organized TiO_2 nanotube arrays fabricated by electrochemical anodization are especially attractive because the tube diameter, length, wall thickness, and crystallization state can be tuned reproducibly through electrolyte chemistry, applied potential, and post-anodization annealing [12-13]. In the context of cardiovascular devices, such polymer-free surface engineering is especially appealing because it seeks to improve the implant-host interface without relying on chronic drug elution or additional carrier layers that may complicate long-term healing.

The biological response to TiO_2 nanotube arrays is not governed by nominal tube diameter alone, but by the coupled effects of local contact geometry, crystallinity, surface energy, and defect chemistry. Previous studies have shown that nanotopographic cues can bias endothelial cell and smooth muscle cell competition, which is highly relevant to restenosis control [14-15]. In the present study, the average inner diameter of approximately 85 ± 7 nm should therefore be interpreted together with the wall/rim geometry of the open-mouth nanotube array. As shown in Table 2, the average wall thickness was approximately 15 ± 3 nm, which is below 30 nm. For adsorbing proteins and adherent endothelial cells, the initial solid-contact regions are not the empty tube opening itself but the nanotube rim and the near-opening inner wall; therefore, the local contact features presented at the pore mouth are closer to the tube-wall scale than to the full inner diameter. This wall-scale interpretation provides a more direct structural basis for considering the present surface as an endothelialization-compatible nanotopography when it is paired with anatase-rich crystallinity and favorable surface chemistry [16-17].

Beyond nanotopography, the crystal phase of TiO_2 strongly modulates hydroxylation, surface polarity, hydration structure, and the adsorption state of biomolecules. As-anodized nanotubes are typically amorphous and require post-treatment to generate anatase- or rutile-containing surfaces [18-19]. Anatase-rich layers formed at moderate annealing temperatures generally exhibit stronger polar interfacial interactions and a more favorable hydration environment, whereas rutile-containing surfaces formed at higher temperatures can alter these interactions and partly attenuate the pro-healing response [16]. Such phase-dependent changes are highly relevant because the earliest hydration and adsorption events influence both subsequent endothelial behavior and the longer-term biointegration of stent surfaces [20-23]. Accordingly, understanding how anatase-rich and mixed-phase nanotube layers differ at the level of interfacial water organization, protein selectivity, and cell-facing signaling remains essential for rational surface design, even before full device-level validation is attempted.

Recent literature has also emphasized that nanotubular materials represent a broadly tunable class of interfaces across biomedical and adjacent interfacial-engineering applications. In addition to cardiovascular TiO_2 systems, tubular nano-architectures have recently been exploited for selective adsorption, protein handling, and catalytic interfacial regulation in separation-oriented platforms [24-31]. Although those reports are not vascular models, they reinforce the broader principle that wall chemistry, shell thickness, accessible pore openings, and surface defect states can be deliberately tuned to control adsorption and transport. Accordingly, the present study compares as-anodized, 450 °C annealed, and 600 °C annealed nanotube layers on Ti-6Al-4V using flat

10.57647/jnsc.2026.1605.22

coupons as a controlled model that isolates phase- and topography-dependent interfacial responses before translation to curved stent geometries. We combined structural characterization with wettability analysis, competitive protein adsorption, and endothelial assays to determine whether a specific crystalline state can provide a superior drug-free, stent-relevant interface. Direct blood-contact testing and flow-based validation remain future tasks, and these translational boundaries are discussed explicitly below. The central aim of the present work is therefore not to claim exhaustive device-level validation, but to identify the crystalline-state window that best aligns interfacial selectivity with endothelial compatibility on a clinically relevant titanium alloy substrate.

From a device-design perspective, an effective stent surface must satisfy two partially competing requirements. On the one hand, the interface should resist nonspecific fouling and avoid presenting strongly activating protein states at the earliest stage of implantation. On the other hand, it should support rapid colonization by endothelial cells so that the metallic substrate is quickly converted into a biologically regulated vascular lining. This dual requirement explains why surface wettability, model protein adsorption, and endothelialization were treated here as complementary readouts rather than as isolated endpoints. A surface that performs well in only one of these dimensions may still fail to promote durable vascular integration if its broader interfacial behavior is unbalanced. On this basis, the present work asks whether moderate thermal crystallization can place TiO_2 nanotube arrays in an interfacial window where nanotopography, crystal phase, and defect chemistry reinforce rather than counteract one another. The comparison among TNT-As, TNT-450, and TNT-600 is especially informative because the three nanotube groups share a common fabrication route and broadly similar geometry, while differing in crystallinity and near-surface chemical state. This design allows the role of phase engineering to be examined more directly than in studies where geometry and chemistry change simultaneously.

2. Materials and Methods

2.1. Substrate Preparation

Flat sheets of medical-grade Ti-6Al-4V alloy (ASTM F136, 0.5 mm thickness) were used as the substrate material for this study. This coupon geometry was intentionally selected as a controlled model to minimize curvature-dependent confounders, enable uniform anodization and surface characterization, and allow side-by-side biological testing of surfaces with identical processing history. Such flat-substrate screening is commonly used at the mechanism-evaluation stage before transfer to expanded or curved stent geometries. The sheets were cut into 10 mm × 10 mm square samples. To replicate the surface finishing state typically required for cardiovascular devices, a multi-stage polishing protocol was applied to the specimens. The samples were initially subjected to mechanical grinding with silicon carbide abrasive papers in a descending sequence of grit sizes (400, 800, 1200, and 2000 grit).

This was followed by fine polishing using 1.0 μm and 0.3 μm alumina slurries on a polishing cloth to produce a mirror-like finish. Post-polishing, the substrates were ultrasonically cleaned in acetone, ethanol, and deionized water for 15 minutes per solvent, dried under nitrogen, and stored in a desiccator before further processing. These polished samples served as the bare titanium control group (Bare-Ti).

2.2. Fabrication of TiO_2 Nanotube Arrays

The synthesis of TiO_2 nanotube arrays was carried out by potentiostatic electrochemical anodization using a two-electrode configuration [32]. The prepared Ti-6Al-4V specimen served as the anode (working electrode), while a platinum foil (20 mm × 20 mm) served as the cathode (counter electrode), with a fixed inter-electrode distance of 2 cm. An ethylene glycol-based electrolyte containing 0.3 wt% NH_4F and 2 vol% deionized water was selected because limited water content and fluoride-assisted dissolution are known to promote self-ordered nanotube growth with open tube mouths on titanium alloys.

The anodization potential of 40 V was chosen to target a stable tube diameter in the approximately 80-100 nm range without excessive over-etching, and the 1 hour duration was selected to generate a continuous micrometer-scale nanotube layer while preserving structural integrity, in line with benchmark anodization studies and recent crystallization-oriented TNT work [13, 19, 32-33]. Under regulation of a DC power source (Agilent E3648A), anodization was conducted at 20 °C. After anodization, the specimens were rinsed thoroughly with ethanol and deionized water to remove residual electrolyte from the nanotubular channels, followed by nitrogen drying. These samples are referred to as the as-anodized group (TNT-As).

2.3. Thermal Annealing Treatment

To induce crystallization of the amorphous as-prepared nanotube arrays, the TNT-As samples underwent thermal annealing in a muffle furnace under ambient air. The specimens were placed in a ceramic crucible and heated at 5 °C/min to either 450 °C or 600 °C, held for 2 hours, and allowed to cool naturally to room temperature inside the furnace [19, 34-35].

10.57647/jnsc.2026.1605.22

The 450 °C condition was selected to favor predominantly anatase crystallization while preserving the tubular architecture, whereas 600 °C was chosen as a higher-temperature condition expected to initiate partial anatase-to-rutile transformation and thereby provide a mixed-phase comparison. These groups are referred to as TNT-450 and TNT-600, respectively. A summary of the fabrication parameters for all experimental groups is provided in Table 1.

2.4. Surface Wettability and Competitive Protein Adsorption

Competitive protein adsorption was analyzed using sterilized specimens incubated for 2 hours at 37 °C with commercially obtained albumin or fibrinogen solutions prepared in PBS under identical conditions. After gentle rinsing to remove loosely bound protein, the retained protein was quantified using commercial ELISA kits according to the manufacturer's instructions and normalized to specimen area.

The relative albumin-versus-fibrinogen adsorption behavior was used as a controlled interfacial indicator rather than as a full plasma simulation. The two model proteins were evaluated under matched buffer and incubation conditions so that differences among the sample groups could be attributed primarily to the surface state rather than to differences in bulk medium composition.

Surface wettability was evaluated by sessile-drop contact-angle measurements at room temperature using 3 μL deionized water droplets. At least three independent droplets were analyzed on each specimen, and the reported values represent the average equilibrium contact angle.

This reduced assay set was selected to provide non-donor-dependent interfacial metrics that can be directly related to crystallinity, hydration, and endothelial response.

Accordingly, the protein adsorption experiment should be interpreted as a mechanistic model of interfacial selectivity rather than a substitute for more complex circulating-fluid testing.

2.5. In Vitro Endothelialization Assays

Commercial Human Umbilical Vein Endothelial Cells (HUVECs; PromoCell GmbH, Heidelberg, Germany; Cat. No. IV-3285) were used to assess the cytocompatibility and pro-endothelialization potential of the surfaces. The HUVECs were maintained in Dulbecco's Modified Eagle Medium supplemented with 10% fetal bovine serum and 1% penicillin-streptomycin under standard incubation conditions (37 °C, 5% CO_2). Prior to cell seeding, all specimens were sterilized by UV irradiation.

HUVECs were selected because rapid recovery of a functional endothelial layer is essential for limiting thrombotic risk and neointimal hyperplasia after stent implantation. Commercially supplied HUVECs were chosen to provide a standardized endothelial model suitable for comparative surface screening.

Because the cells were obtained as commercially supplied, de-identified cell products and no human participants, identifiable human specimens, animals, or clinical interventions were involved, institutional ethical approval was not required for this in vitro surface-screening study.

For the proliferation assay, HUVECs were seeded onto the specimens at a density of 2×10^4 cells per well in 24-well plates. Cell viability was measured after 1, 3, and 5 days using the Cell Counting Kit-8 protocol, and absorbance was recorded at 450 nm. For fluorescence-based morphological observation, HUVECs were seeded at the same density and cultured for 72 hours, followed by fixation in 4% paraformaldehyde, permeabilization with 0.1% Triton X-100, and staining with DAPI and rhodamine-phalloidin to visualize nuclei and F-actin, respectively.

Fluorescence images were collected with a Leica DMI8 microscope and were used to compare cell spreading, actin organization, and surface coverage qualitatively among the tested groups.

Together, the proliferation and morphology assessments were intended to distinguish surfaces that merely permit cell survival from those that more actively support endothelialization-relevant spreading behavior.

Table 1. Summary of anodization and annealing parameters for the experimental sample groups

Sample ID	Substrate Material	Anodization Voltage (V)	Anodization Time (hr)	Electrolyte Composition	Annealing Temp. (°C)	Annealing Time (hr)
Bare-Ti	Ti-6Al-4V	-	-	-	-	-
TNT-As	Ti-6Al-4V	40	1	EG + 0.3% NH_4F + 2% H_2O	-	-
TNT-450	Ti-6Al-4V	40	1	EG + 0.3% NH_4F + 2% H_2O	450	2
TNT-600	Ti-6Al-4V	40	1	EG + 0.3% NH_4F + 2% H_2O	600	2

10.57647/jnsc.2026.1605.22

3. Results and Discussion

3.1. Surface Morphology and Topography Characterization

The surface morphology of the prepared samples was systematically investigated using FESEM, and the results are presented in Fig. 1. The Bare-Ti control sample exhibited a relatively smooth and featureless surface, with only minor parallel grooves remaining from the mechanical polishing process (Fig. 1a). Following electrochemical anodization, a dramatic transformation of the surface was observed.

The TNT-As sample (Fig. 1b) was uniformly covered with a highly dense and well-ordered layer of vertically aligned TiO_2 nanotubes. The nanotubes possessed distinct circular openings, forming a nanoporous structure. After annealing at 450 °C (Fig. 1c) and 600 °C (Fig. 1d), the nanotubular architecture remained intact without any significant collapse or cracking, demonstrating the excellent thermal stability of the TNT arrays.

This structural integrity is crucial for maintaining the desired nanotopography after the necessary crystallization step [27]. High-magnification images reveal that the pore edges of the annealed samples appear slightly more defined and sintered compared to the as-anodized nanotubes, which can be attributed to the thermal treatment. To further quantify the dimensions of the nanotube arrays, cross-sectional FESEM images were acquired (Fig. 2).

These images clearly show vertically oriented nanotube layers strongly attached to the underlying Ti-6Al-4V substrate. A continuous interface was observed between the metallic substrate and the nanotubular layer, indicating stable adhesion after anodization and after subsequent annealing. This interfacial continuity is important because a stent coating must remain adherent during subsequent handling and deployment. Based on the cross-sectional analysis, the nanotubes exhibited a mean length of 1.9 ± 0.2 μm. The high aspect ratio increases the available interfacial area for protein and cell interactions. At the same time, because dedicated expansion, fatigue, and corrosion-adhesion tests were not performed here, the preserved morphology should be interpreted as encouraging structural evidence rather than definitive proof of deployment-level mechanical robustness.

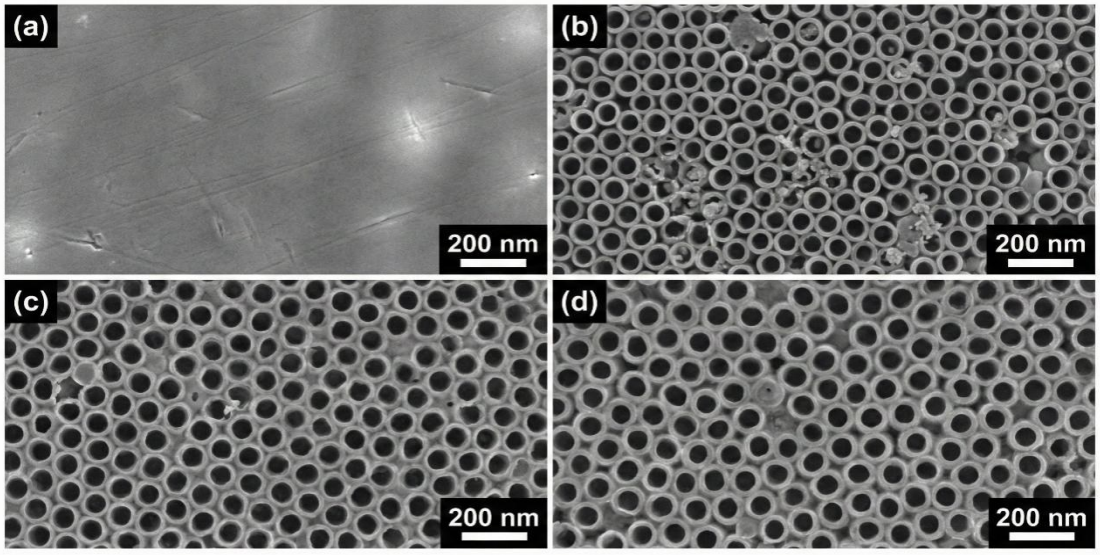

Figure 1. Low-magnification (×10,000) FESEM top-view images of the sample surfaces. (a) Bare-Ti. (b) TNT-As. (c) TNT-450. (d) TNT-600

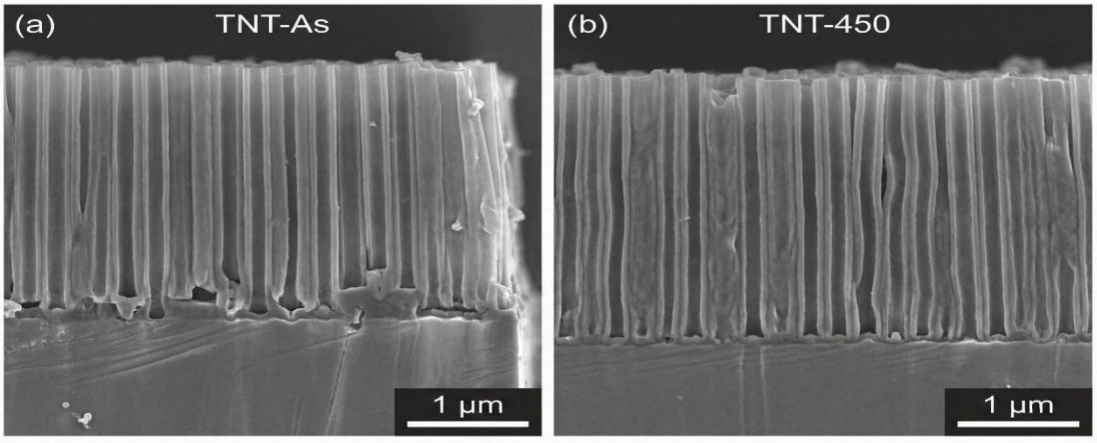

Figure 2. Cross-sectional FESEM images of the TiO_2 nanotube arrays. (a) TNT-As sample. (b) TNT-450 sample

10.57647/jnsc.2026.1605.22

The dimensional parameters of the nanotubes derived from FESEM analysis are summarized in Table 2. The average inner diameter of the nanotubes for all TNT groups was approximately 85 ± 7 nm, and the wall thickness was about 15 ± 3 nm. These dimensions are primarily dictated by the anodization potential of 40 V and agree with previous reports showing that nanotube diameter scales with applied potential [33, 36].

Importantly, thermal annealing did not significantly alter the tube diameter or wall thickness, confirming that the key geometric features were established during anodization. The present material should be considered a firmly attached TiO_2 nanotube array rather than detached nanotube powder.

Therefore, the biologically relevant interface is the open-mouth array exposed to proteins and cells, with both the rim and the near-opening inner walls contributing to wetting, protein exchange, and cell-substrate contact. In this geometry, the empty pore diameter does not by itself define the contact scale: adsorbing proteins and spreading endothelial cells initially encounter the nanotube rim, the tube-wall edge, and the near-opening inner wall. Because the measured wall thickness was only about 15 ± 3 nm, the local solid-contact features presented at the pore mouth are below 30 nm even though the inner opening is approximately 85 nm. This rim/wall-scale explanation provides a more direct structural basis for the observed endothelial compatibility than a diameter-only argument, while the comparison among TNT-As, TNT-450, and TNT-600 further indicates that this geometry must act together with crystallinity and surface chemistry [16-17].

The detailed nanostructure and crystallinity were further examined by TEM. Fig. 3 presents the low-magnification TEM image of nanotubes detached from the TNT-450 surface, confirming their hollow tubular structure.

High-resolution TEM and selected-area electron diffraction (SAED) provided direct evidence of the crystalline state after annealing. The HRTEM image of the TNT-450 nanotube wall (Fig. 4a) shows clear lattice fringes with a d-spacing of 0.352 nm, corresponding to the anatase (101) plane.

Table 2. Morphological parameters of TiO_2 Nanotube arrays measured from FESEM and TEM images

Sample Group	Average Inner Diameter (nm)	Average Wall Thickness (nm)	Average Length (μm)
TNT-As	86 ± 8	16 ± 2	1.9 ± 0.2
TNT-450	85 ± 7	15 ± 3	1.8 ± 0.3
TNT-600	84 ± 9	15 ± 2	1.9 ± 0.2

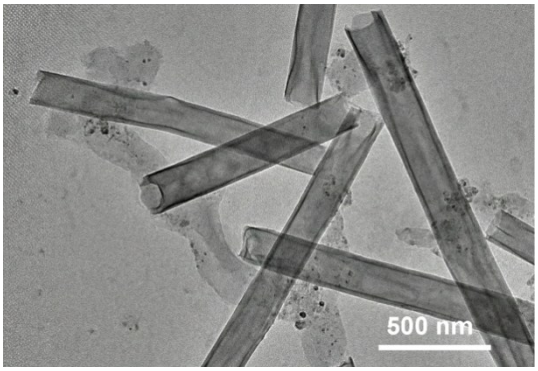

Figure 3. Representative low-magnification TEM image of detached TiO_2 nanotubes from the TNT-450 sample, showing the hollow high-aspect-ratio tubular morphology

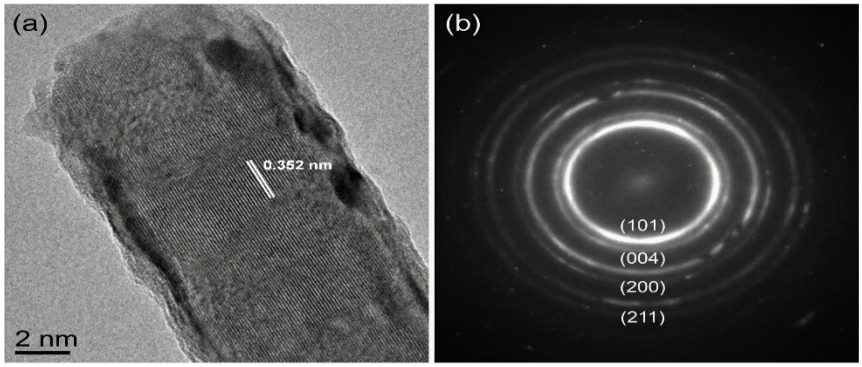

Figure 4. High-resolution structural analysis of the TNT-450 sample. (a) HRTEM image of a nanotube wall with the 0.352 nm lattice-fringe spacing assigned to anatase (101) explicitly marked. (b) Corresponding SAED pattern showing diffraction rings characteristic of polycrystalline anatase

10.57647/jnsc.2026.1605.22

The corresponding SAED pattern (Fig. 4b) displays concentric rings that can be indexed to the (101), (004), (200), and (211) planes of anatase [37]. In contrast, the TNT-As specimen exhibited diffuse diffraction features consistent with an amorphous wall, while the TNT-600 specimen displayed mixed lattice domains and SAED signatures attributable to both anatase and rutile. These TEM observations directly support the conclusion that annealing at 450 °C yields a predominantly anatase nanotube layer, whereas 600 °C initiates the anatase-to-rutile transition while retaining the tubular morphology. The surface topography at the nanoscale was assessed by AFM, as shown in Fig. 6. The three-dimensional maps illustrate the pronounced increase in surface complexity and roughness after nanotube formation. The Bare-Ti surface remained relatively flat, whereas the TNT surfaces displayed a textured landscape defined by nanotube openings. The quantitative roughness parameters presented in Table 3 show an increase in Ra from 4.2 ± 0.5 nm for Bare-Ti to 25.8 ± 2.1 nm for TNT-As. Annealing caused a modest additional increase, with TNT-450 and TNT-600 exhibiting Ra values of 28.3 ± 2.5 nm and 29.1 ± 2.8 nm, respectively. Such changes indicate that annealing preserved the nanotopography while subtly modifying the surface microtexture.

However, the biological response observed in this work cannot be attributed to roughness alone, because the annealed nanotube groups had similar roughness values but distinct crystallinity, wettability, and protein adsorption profiles.

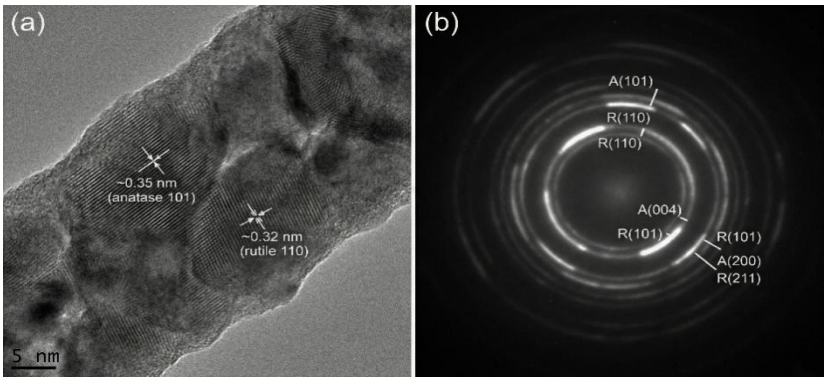

Figure 5. High-resolution structural analysis of the TNT-600 sample. (a) HRTEM image revealing the presence of both anatase (A) and rutile (R) crystallites within the nanotube wall. (b) The corresponding SAED pattern with diffraction rings indexed to both anatase and rutile phases, confirming a mixed-phase structure

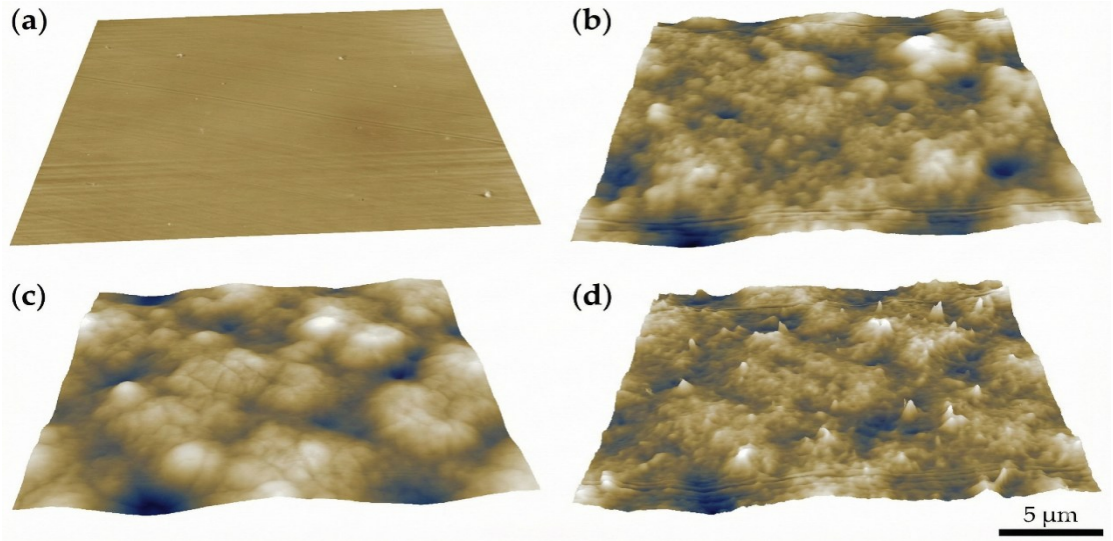

Figure 6. 3D AFM topographical images (5 µm × 5 µm) of the four sample groups. (a) Bare-Ti. (b) TNT-As. (c) TNT-450. (d) TNT-600

Table 3. Surface roughness parameters and static water contact angles for the different sample groups

Sample ID	Average Roughness (Ra) (nm)	Root-Mean-Square Roughness (Rq) (nm)	Water Contact Angle (°)
Bare-Ti	4.2 ± 0.5	5.5 ± 0.6	78.5 ± 3.2
TNT-As	25.8 ± 2.1	32.4 ± 2.5	55.1 ± 4.1
TNT-450	28.3 ± 2.5	35.8 ± 3.0	12.6 ± 2.8
TNT-600	29.1 ± 2.8	36.5 ± 3.2	34.7 ± 3.5

10.57647/jnsc.2026.1605.22

3.2. Crystalline Structure and Phase Composition Analysis

To identify the crystal structure of the TNT layers, XRD analysis was performed and the patterns are shown in Fig. 7. The diffractogram of the Bare-Ti substrate exhibits characteristic peaks of the α and β phases of Ti-6Al-4V. For TNT-As, the absence of new TiO_2 reflections beyond the metallic substrate confirms the poorly crystalline or amorphous nature of the as-anodized nanotubes, in agreement with the TEM and Raman observations [19, 38]. Annealing produced clear phase-dependent changes in the XRD patterns. The TNT-450 sample showed a prominent peak at $2\theta = 25.3°$, corresponding to the anatase (101) reflection. Additional weaker anatase signals, including the (004) reflection at 37.8° and the (200) reflection at 48.0°, were also detected. The weaker 48.0° anatase feature is explicitly annotated in the figure to improve readability. No rutile peaks were observed for TNT-450, indicating the formation of a predominantly phase-pure anatase nanotube layer [18]. In contrast, TNT-600 exhibited both anatase and rutile reflections. In addition to the anatase (101) peak, a rutile (110) signal emerged at 27.4°, and this weak rutile peak is also highlighted in the figure. The coexistence of both phases confirms that annealing at 600 °C initiated the thermodynamically favored anatase-to-rutile transformation.

Although the FESEM cross-sections did not reveal gross delamination or collapse, the higher-temperature treatment likely produced a more thermally transformed oxide/substrate interface, which may become relevant under long-term loading or corrosion conditions. The relative rutile fraction in TNT-600 was estimated to be approximately 32% using the Spurr-Myers relationship. Raman spectroscopy, which is highly sensitive to local vibrational modes, was used to corroborate the XRD findings.

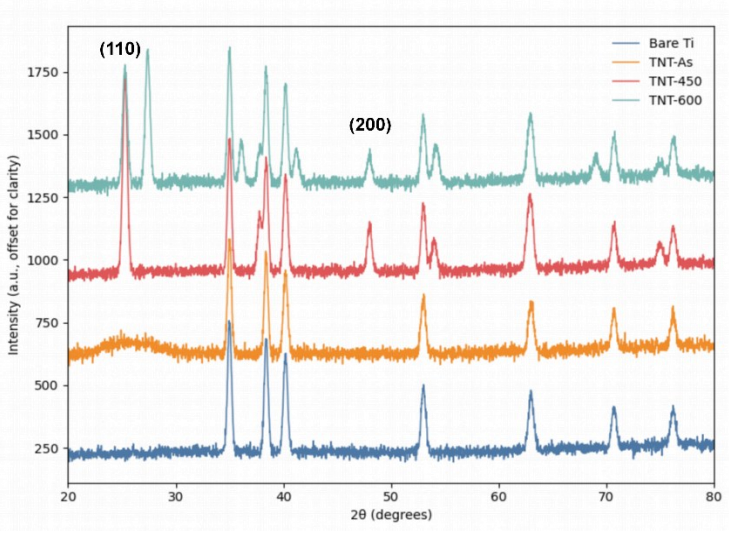

Figure 7. XRD patterns of the Bare-Ti, TNT-As, TNT-450, and TNT-600 samples. TNT-450 shows an anatase-dominated pattern, whereas TNT-600 shows a mixed anatase/rutile pattern. The weaker anatase (200) reflection at 48.0° and rutile (110) reflection at 27.4° are marked in the plot for clarity

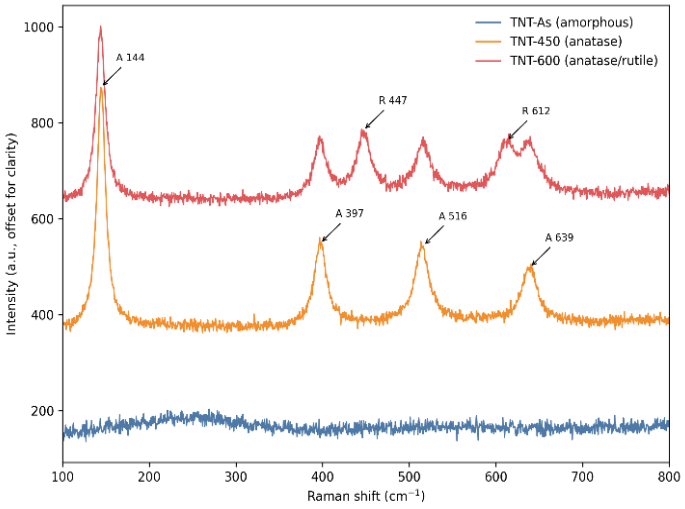

Figure 8. Raman spectra of the TNT-As, TNT-450, and TNT-600 samples. The spectra confirm the amorphous nature of TNT-As, the pure anatase structure of TNT-450, and the mixed anatase/rutile phase of TNT-600

10.57647/jnsc.2026.1605.22

The TNT-As specimen did not exhibit identifiable Raman reflections, consistent with its amorphous character. The TNT-450 spectrum showed intense peaks at 144 cm^{-1}, 397 cm^{-1}, 516 cm^{-1}, and 639 cm^{-1}, corresponding to the characteristic anatase vibrational modes. For TNT-600, additional peaks at 447 cm^{-1} and 612 cm^{-1} appeared alongside the anatase signals, indicating the presence of rutile. The coexistence of anatase and rutile modes provides complementary evidence for the mixed-phase structure of TNT-600, while the sharper peaks observed after annealing confirm an increase in crystallinity.

3.3. Surface Chemical State and Wettability

To ascertain the chemical valence states and surface elemental composition, XPS analysis was performed because these features are directly relevant to protein adsorption and subsequent cellular interactions. The survey spectra of all TNT specimens were dominated by oxygen (O 1s), titanium (Ti 2p), and adventitious carbon (C 1s) signals. Notably, the TNT-As specimen displayed a minor fluorine (F 1s) peak that can be assigned to residual species from the NH_4F-containing anodization electrolyte.

This fluorine signal disappeared after annealing, indicating effective thermal removal of the residual fluoride-containing species. Even though the residual fluoride level was low, it may still contribute to the different interfacial behavior of TNT-As by modifying surface acidity, hydration, and charge development. The quantitative XPS summary is provided in Table 4.

For all TNT samples, the Ti 2p spectrum could be deconvoluted into Ti $2p_{3/2}$ and Ti $2p_{1/2}$ peaks at approximately 458.8 eV and 464.5 eV, respectively (Figs. 9 and 10). The spin-orbit splitting of 5.7 eV is characteristic of the Ti^{4+} oxidation state in TiO_2 [29]. No meaningful contribution from lower oxidation states was detected, indicating that the outermost surface remained predominantly oxidized.

The high-resolution O 1s spectrum is particularly informative because it captures lattice oxygen, vacancy-related oxygen environments, and surface hydroxyl species (Fig. 10). The O 1s envelopes were deconvoluted into three components: lattice oxygen at approximately 530.1 eV, vacancy-related oxygen environments at approximately 531.5 eV, and hydroxyl/adsorbed-water species at approximately 532.6 eV.

As summarized in Table 4, the relative area of the vacancy-associated component increased from 8.1% for TNT-As to 15.5% for TNT-450 and 18.9% for TNT-600. This trend is consistent with the view that thermal treatment reorganizes the near-surface oxide and generates additional defect-associated sites [29-30]. Importantly, the O 1s distribution also helps rationalize why TNT-As and TNT-450, despite both being hydrophilic, do not exhibit identical biological behavior.

Table 4. Surface elemental composition (atomic %) and deconvoluted O 1s peak areas (%) from XPS analysis

Sample ID	Ti (at. %)	O (at. %)	C (at. %)	F (at. %)	O-Lattice (%)	O-Vacancy (%)	O-Hydroxyl (%)
TNT-As	26.5	54.1	18.2	1.2	75.3	8.1	16.6
TNT-450	28.9	59.8	11.3	-	70.2	15.5	14.3
TNT-600	29.5	61.2	9.3	-	73.8	18.9	7.3

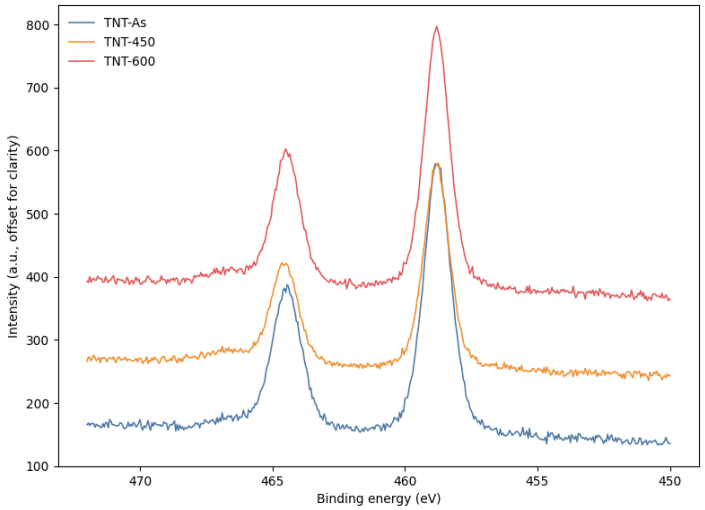

Figure 9. High-resolution XPS spectra of the Ti 2p region for (a) TNT-As, (b) TNT-450, and (c) TNT-600 samples, all showing the characteristic peaks of the Ti^{4+} state in TiO_2

10.57647/jnsc.2026.1605.22

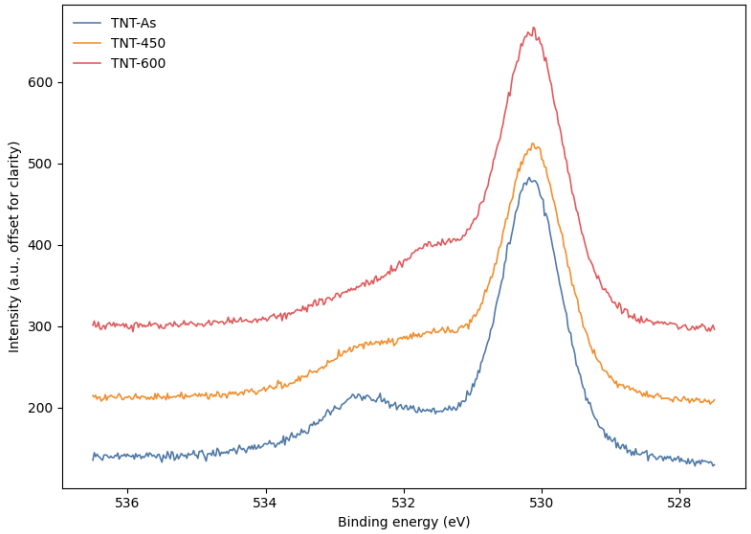

Figure 10. High-resolution XPS spectra of the O 1s region for (a) TNT-As, (b) TNT-450, and (c) TNT-600 samples. The peaks are deconvoluted into components representing lattice oxygen (O-L), oxygen vacancies (O-V), and hydroxyl groups (O-H)

TNT-As retained the highest hydroxyl fraction but a relatively low vacancy fraction and an amorphous framework, whereas TNT-450 combined anatase crystallinity with a moderate increase in vacancy-related sites. This balance may enhance polar surface interactions and protein reorganization without introducing the more strongly transformed oxide state observed after 600 °C treatment. At the same time, oxygen-vacancy-rich surfaces can be a double-edged sword because excessive defect density may promote reactive oxygen species generation in aqueous environments. The present results suggest that the intermediate defect state of TNT-450 is biologically more favorable than either the amorphous TNT-As surface or the more highly defect-rich TNT-600 surface, but direct ROS measurements will be required in future work to confirm this interpretation. Surface wettability is a critical factor governing the earliest liquid-solid interactions on an implanted material. Fig. 11 illustrates the water droplet profiles on the various specimen surfaces, with the corresponding quantitative contact-angle measurements summarized in Table 3. The Bare-Ti substrate displayed moderate hydrophobicity, characterized by a static contact angle of 78.5°.

Upon nanotube formation, the TNT-As specimen transitioned toward a more hydrophilic state (55.1°), likely because of the combined effects of higher surface roughness and a greater density of hydroxyl-associated oxygen species detected by XPS. A much stronger shift in wetting behavior was observed after thermal annealing. The TNT-450 surface became superhydrophilic, with the water droplet spreading almost completely and yielding a contact angle of 12.6°.

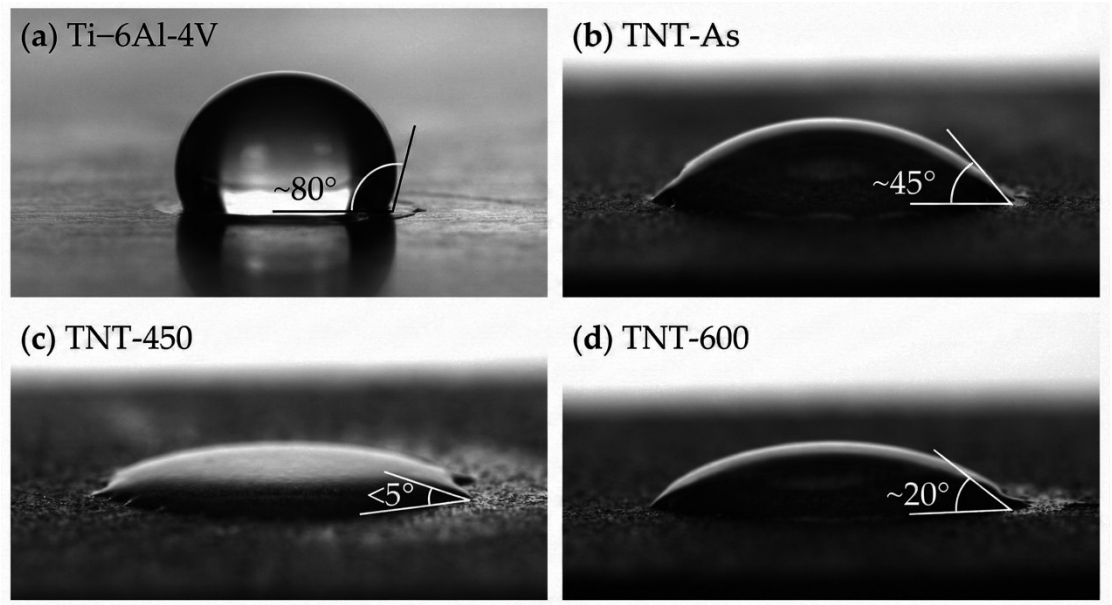

Figure 11. Static water-contact-angle images of (a) Bare-Ti, (b) TNT-As, (c) TNT-450, and (d) TNT-600 surfaces used for wettability analysis. Contact-angle values are reported as mean ± SD (n = 3)

10.57647/jnsc.2026.1605.22

The TNT-600 surface was also distinctly hydrophilic (34.7°), but remained less wettable than TNT-450. This ranking is important because a stable hydration layer can moderate nonspecific interfacial reorganization and support endothelial attachment. Importantly, wettability alone does not explain the full biological ranking, because TNT-As was already more hydrophilic than Bare-Ti yet did not reproduce the protein-adsorption balance or endothelial growth observed for TNT-450. The present data therefore suggest a coupled contribution of crystallinity, defect chemistry, and hydroxyl-mediated surface polarity rather than contact angle alone [16, 20-22]. In other words, annealing does not simply amplify wetting by roughness effects; it also changes the chemical identity of the water-facing surface. This distinction helps explain why TNT-450 outperformed TNT-As despite both being considerably more hydrophilic than Bare-Ti, and why TNT-600, although still strongly wettable, did not preserve the same interfacial advantage as the anatase-rich sample.

3.4. Competitive Protein Adsorption

Protein adsorption is one of the earliest events at the biomaterial-liquid interface and strongly influences subsequent cellular responses. In the present work, albumin and fibrinogen were used as purified model proteins to provide a controlled, reductionist view of interfacial selectivity rather than a full plasma simulation. ELISA quantification showed that Bare-Ti adsorbed relatively high levels of fibrinogen (2.8 ± 0.3 μg/cm²) and less albumin (1.5 ± 0.2 μg/cm²) (Fig. 12). All TNT surfaces shifted this balance in a more favorable direction, and TNT-450 showed the strongest effect, with reduced fibrinogen adsorption (1.1 ± 0.2 μg/cm²) together with increased albumin adsorption (3.2 ± 0.4 μg/cm²). This selective adsorption profile is consistent with a more passivating interfacial state and with the stronger endothelial response observed on TNT-450. At the same time, the difference between TNT-As and TNT-450 indicates that contact angle alone is insufficient to explain the adsorption trend; anatase-rich crystallinity, surface hydroxyl configuration, and moderate defect chemistry likely contribute to a more favorable physicochemical microenvironment for protein organization. Because real plasma contains many additional competing species, the present dataset should be interpreted as a mechanistic snapshot rather than as direct proof of in vivo thrombogenicity [20-23]. A comparison of TNT-As, TNT-450, and TNT-600 is particularly informative because it separates the influence of tube formation from the influence of crystalline-state optimization. TNT-As already provided a rough, hydrophilic nanotubular surface, yet its adsorption selectivity did not match that of TNT-450. This contrast suggests that the anatase-rich surface does more than simply increase wettability; it likely changes the molecular environment encountered by proteins at the interface, including the balance between hydration-mediated repulsion, polar interaction sites, and the organization of surface hydroxyl groups. In this framework, TNT-450 may favor a less activating adsorption state by combining high wetting with a more ordered and chemically balanced oxide surface, whereas TNT-600 may partially lose that advantage because mixed-phase transformation alters the water-facing chemistry of the nanotube walls. This interpretation also helps explain why the protein-adsorption assay remains valuable even though it does not reproduce the full complexity of circulating biomolecule mixtures. As a reductionist screen, it allows the relative tendency of the surfaces toward passivating versus activating interfacial states to be compared under tightly controlled conditions. In real vascular environments, this initial adsorption layer would be further shaped by lipoproteins, globulins, complement factors, flow-dependent mass transport, and continuous molecular exchange. Even so, the present dataset provides a mechanistically meaningful first step for identifying which crystalline state is most worthy of deeper translation-oriented evaluation.

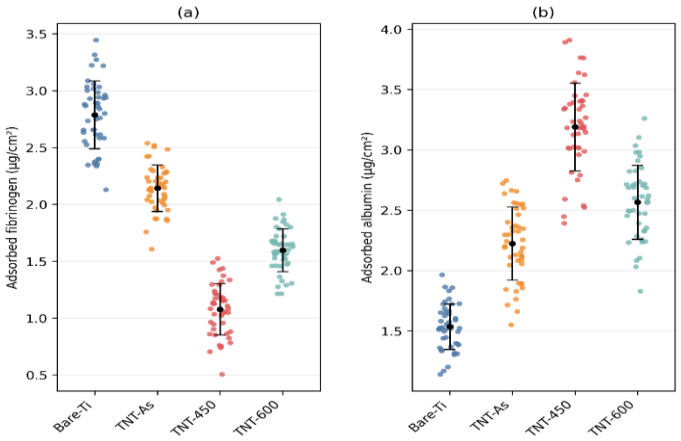

Figure 12. Quantification of protein adsorption on the sample surfaces after 2 hours of incubation. (a) Adsorbed fibrinogen. (b) Adsorbed albumin. Data are mean ± SD (n = 3). Statistical analysis was performed by one-way ANOVA with Tukey's post hoc test; * $p < 0.05$ and ** $p < 0.01$ as indicated in the figure

10.57647/jnsc.2026.1605.22

Table 5. Summary of quantitative wettability, protein adsorption, and endothelialization performance data

Sample ID	Water Contact Angle (°)	Fibrinogen Adsorbed (μg/cm²)	Albumin Adsorbed (μg/cm²)	Albumin/Fibrinogen Ratio	HUVEC Viability at Day 5 (OD_{450})	Overall Interfacial Ranking
Bare-Ti	78.5 ± 3.2	2.8 ± 0.3	1.5 ± 0.2	0.54	0.85 ± 0.07	Baseline
TNT-As	55.1 ± 4.1	2.1 ± 0.2	2.2 ± 0.3	1.05	1.21 ± 0.09	Moderate
TNT-450	12.6 ± 2.8	1.1 ± 0.2	3.2 ± 0.4	2.91	1.85 ± 0.11	Best
TNT-600	34.7 ± 3.5	1.6 ± 0.2	2.5 ± 0.3	1.56	1.48 ± 0.10	Good

A summary of the key non-donor-dependent interfacial and endothelialization metrics is provided in Table 5 for direct comparison. Across contact angle, competitive protein adsorption, and endothelial proliferation, TNT-450 consistently provided the most favorable overall balance of responses.

Table 5 emphasizes that TNT-450 was not merely the best-performing group in a single isolated test, but the only surface that consistently occupied the most favorable position across wetting, model-protein selectivity, and endothelial proliferation. This convergence is important because biomaterial optimization often fails when gains in one interfacial property are offset by losses in another. Here, the coordinated improvement across multiple readouts supports the view that moderate annealing produces a genuinely advantageous surface state rather than an artifact of one measurement.

3.5. In Vitro Endothelialization

Rapid re-endothelialization is crucial for long-term stent success because a functional endothelial layer provides the most stable anti-fouling vascular interface and helps regulate vascular tone and remodeling. HUVEC proliferation on the different surfaces was monitored over 5 days using the CCK-8 assay (Fig. 13). On day 1, viability was comparable across all groups, indicating similar initial attachment. From day 3 onward, however, clear differences emerged. Cells on the TNT surfaces proliferated faster than those on Bare-Ti, and TNT-450 consistently showed the highest growth rate. By day 5, the optical density for TNT-450 (1.85 ± 0.11) was more than double that of Bare-Ti (0.85 ± 0.07) and significantly higher than TNT-As (1.21 ± 0.09) and TNT-600 (1.48 ± 0.10). These findings indicate that the anatase-rich nanotubular surface provides an especially favorable substrate for endothelial expansion [16-17]. The result also places the approximately 85 nm inner diameter in a more precise geometric context. Endothelial cells do not attach to an empty cylindrical void; they spread across the solid rim, wall edge, and near-opening wall surfaces of the ordered array. Because the measured wall thickness was approximately 15 ± 3 nm, the local solid features available at the tube mouth fall below 30 nm, which provides a plausible contact-scale explanation for why endothelial proliferation was not hindered by the larger opening size. The data therefore support a combined interpretation in which thin tube walls, preserved open-mouth architecture, anatase-rich crystallinity, and hydration-favorable chemistry jointly define the endothelialization response.

The endothelialization trend is mechanistically consistent with the interfacial data discussed above. A surface that maintains strong hydration, discourages an excessively fibrinogen-favoring adsorption pattern, and presents a stable anatase-rich oxide is expected to offer a more permissive microenvironment for endothelial attachment and subsequent expansion. In this respect, TNT-450 appears to balance topography and chemistry more effectively than TNT-As or TNT-600. The amorphous TNT-As surface provided some benefit over Bare-Ti, but its weaker adsorption selectivity and lower degree of crystalline organization may limit the maturation of a cell-supportive interface. TNT-600, by contrast, remained favorable overall but likely reflects the trade-off introduced by stronger thermal transformation and mixed-phase chemistry.

At the translational level, proliferation should be interpreted as a strong but partial indicator of endothelialization. Rapid surface coverage is highly desirable because it shortens the period during which the metallic implant remains directly exposed to circulating components, yet endothelial quality also depends on cell spreading, junction formation, nitric-oxide-related function, inflammatory phenotype, and adaptation to shear. The current data therefore identify TNT-450 as the most promising surface for deeper endothelial studies, while also defining clear next-step assays such as migration, barrier-marker expression, and flow-conditioned endothelial behavior. This more cautious framing is fully consistent with the intended role of the present study as a phase-engineering screen on flat Ti-6Al-4V substrates.

Equally important, the present endothelialization result strengthens the practical argument for crystalline-state engineering as a device-relevant design lever. Stent surfaces are exposed to a narrow and demanding biological sequence: an initially acellular metallic interface must transition rapidly into a cell-regulated surface without provoking excessive interfacial activation during the early healing window.

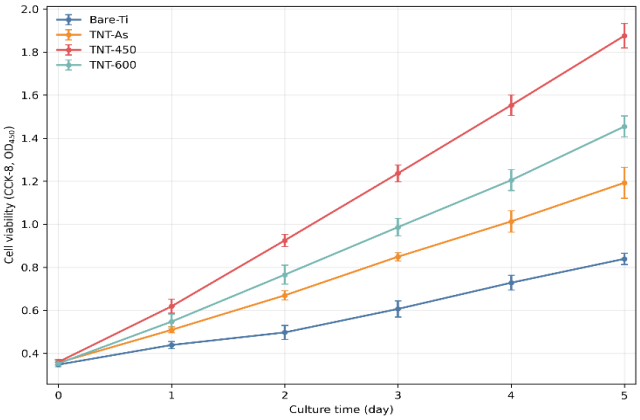

Figure 13. HUVEC proliferation on the different sample surfaces over 5 days, as measured by the CCK-8 assay. Data are mean ± SD (n = 5). Statistical analysis was performed by one-way ANOVA with Tukey's post hoc test; * $p < 0.05$, ** $p < 0.01$, and *** $p < 0.001$ as indicated in the figure

In that setting, a material that simultaneously supports ordered hydration, favorable model-protein organization, and robust endothelial expansion is inherently attractive. The data therefore suggest that the benefit of TNT-450 is not limited to a single in vitro endpoint, but may reflect a broader convergence between physicochemical surface state and vascular-healing compatibility.

4. Conclusion

Well-ordered TiO_2 nanotube arrays were successfully fabricated on Ti-6Al-4V and their crystalline state was tuned by post-anodization annealing. Moderate annealing at 450 °C generated a predominantly anatase nanotube layer while preserving the ordered morphology, whereas 600 °C induced a mixed anatase/rutile state and a more thermally transformed interface. Across the retained structural analyses, TNT-450 consistently combined phase purity, preserved nanotube architecture, favorable oxygen-state distribution, and the strongest wetting response. Within the present assay set, TNT-450 provided the best overall balance of interfacial and biological properties, including superhydrophilicity, favorable albumin-over-fibrinogen adsorption, and enhanced HUVEC proliferation. This performance likely arises from the combined effect of ordered nanotopography, anatase-dominated crystallinity, moderate vacancy-related surface defects, and a more favorable interfacial hydration environment. Importantly, the comparison among Bare-Ti, TNT-As, TNT-450, and TNT-600 indicates that neither nanotopography alone nor hydrophilicity alone is sufficient to explain the biological ranking. Instead, the most favorable response was observed when the nanotube geometry was paired with an anatase-rich, chemically balanced surface state.These findings support crystalline-phase engineering of TiO_2 nanotube arrays as a promising drug-free strategy for improving stent-surface biointegration and endothelialization. However, the conclusions remain limited to flat-substrate characterization, model-protein adsorption, and static endothelial assays. Thus, the present work should be regarded as a mechanism-oriented screening study that identifies a favorable interfacial design window rather than as a final device-validation report. Direct dynamic blood-contact, flow-based, deformation-tolerant stent-form, and longer-term in vivo studies will be required before translational claims can be extended to clinical devices. Future work should also assess endothelial function more comprehensively through migration, junction formation, inflammatory signaling, and shear adaptation, thereby linking the current surface-engineering insights to a more complete vascular-healing framework.

Author Contributions

C.F. contributed to conceptualization, methodology, investigation, data curation, formal analysis, visualization, and writing – original draft preparation. L.C. contributed to investigation, data curation, formal analysis, and visualization. F.L. contributed to conceptualization, supervision, project administration, funding acquisition, and writing – review & editing. All authors have read and agreed to the published version of the manuscript.

Availability of Data and Materials

The data supporting the findings of this study are available from the corresponding author upon reasonable request.

Conflict of Interest

The authors declare that they have no known competing financial interests or personal relationships that could have appeared to influence the work reported in this paper.

Funding

R&D Center for Synthetic Biology and Green Biomanufacturing Technology, R&D Program of Jinan City, Shandong, China (Grant No. 202534063)

Ethical Approval

This study used commercially sourced HUVECs for in vitro biomaterial surface screening. No human participants were recruited, no identifiable human specimens were collected, and no animal experiments or clinical interventions were performed. Therefore, institutional ethical approval was not applicable to the present study.

References

[1] Simard, T.; Hibbert, B.; Ramirez, F. D.; Froeschl, M.; Chen, Y.-X.; O'Brien, E. R. The Evolution of Coronary Stents: A Brief Review. *Can. J. Cardiol.*, **30**, 35-45 (2014).

[2] Lowe, H. C.; Oesterle, S. N.; Khachigian, L. M. Coronary In-Stent Restenosis: Current Status and Future Strategies. *J. Am. Coll. Cardiol.*, **39**, 183-193 (2002).

[3] Joner, M.; Finn, A. V.; Farb, A.; Mont, E. K.; Kolodgie, F. D.; Ladich, E.; Kutys, R.; Skorija, K.; Gold, H. K.; Virmani, R. Pathology of Drug-Eluting Stents in Humans: Delayed Healing and Late Thrombotic Risk. *J. Am. Coll. Cardiol.*, **48**, 193-202 (2006).

[4] Finn, A. V.; Nakazawa, G.; Joner, M.; Kolodgie, F. D.; Mont, E. K.; Gold, H. K.; Virmani, R. Vascular Responses to Drug Eluting Stents. *Arterioscler. Thromb. Vasc. Biol.*, **27**, 1500-1510 (2007).

[5] Rizas, K. D.; Mehilli, J. Stent Polymers: Do They Make a Difference? *Circ. Cardiovasc. Interv.*, **9**, e002943 (2016).

[6] Otsuka, F.; Finn, A. V.; Yazdani, S. K.; Nakano, M.; Kolodgie, F. D.; Virmani, R. The Importance of the Endothelium in Atherothrombosis and Coronary Stenting. *Nat. Rev. Cardiol.*, **9**, 439-453 (2012).

[7] Meyers, S. R.; Kenan, D. J.; Khoo, X.; Grinstaff, M. W. A Bioactive Stent Surface Coating That Promotes Endothelialization While Preventing Platelet Adhesion. *Biomacromolecules*, **12**, 533-539 (2011).

[8] Niinomi, M. Mechanical Properties of Biomedical Titanium Alloys. *Mater. Sci. Eng. A*, **243**, 231-236 (1998).

[9] Sidambe, A. T. Biocompatibility of Advanced Manufactured Titanium Implants-A Review. *Materials*, **7**, 8168-8188 (2014).

[10] Barberi, J.; Spriano, S. Titanium and Protein Adsorption: An Overview of Mechanisms and Effects of Surface Features. *Materials*, **14**, 1590 (2021).

[11] Manivasagam, V. K.; Sabino, R. M.; Kantam, P.; Popat, K. C. Surface Modification Strategies to Improve Titanium Hemocompatibility: A Comprehensive Review. *Mater. Adv.*, **2**, 5824-5842 (2021).

[12] Macak, J. M.; Tsuchiya, H.; Ghicov, A.; Yasuda, K.; Hahn, R.; Bauer, S.; Schmuki, P. TiO_2 Nanotubes: Self-Organized Electrochemical Formation, Properties and Applications. *Curr. Opin. Solid State Mater. Sci.*, **11**, 3-18 (2007).

[13] Fu, Y.; Mo, A. A Review on the Electrochemically Self-Organized Titania Nanotube Arrays: Synthesis, Modifications, and Biomedical Applications. *Nanoscale Res. Lett.*, **13**, 187 (2018).

[14] Xin, W.; Meng, C.; Jie, W.; Junchao, T.; Yan, S.; Ning, D. Morphology Dependence of TiO_2 Nanotube Arrays on Anodization Variables and Buffer Medium. *J. Semicond.*, **31**, 063003 (2010).

[15] Brammer, K. S.; Oh, S.; Gallagher, J. O.; Jin, S. Enhanced Cellular Mobility Guided by TiO_2 Nanotube Surfaces. *Nano Lett.*, **8**, 786-793 (2008).

[16] Zhang, J.; Ren, K.; Qiu, J.; Chen, B.; Duan, W.; Liu, J.; Li, G.; Li, D. Nanotexture and Crystal Phase Regulation for Synergistic Enhancement in Re-Endothelialization on Medical Pure Titanium Surface. *Mater. Today Bio*, **25**, 100968 (2024).

[17] Peng, L.; Eltgroth, M. L.; LaTempa, T. J.; Grimes, C. A.; Desai, T. A. The Effect of TiO_2 Nanotubes on Endothelial Function and Smooth Muscle Proliferation. *Biomaterials*, **30**, 1268-1272 (2009).

[18] Benčina, M.; Iglič, A.; Mozetič, M.; Junkar, I. Crystallized TiO_2 Nanosurfaces in Biomedical Applications. *Nanomaterials*, **10**, 1121 (2020).

[19] Wang, Z.; Chen, K.; Xue, D. Crystallization of Amorphous Anodized TiO_2 Nanotube Arrays. *RSC Adv.*, **14**, 8195-8203 (2024).

[20] Barberi, J.; Mandrile, L.; Napione, L.; Giovannozzi, A. M.; Rossi, A. M.; Vitale, A.; Yamaguchi, S.; Spriano, S. Albumin and Fibronectin Adsorption on Treated Titanium Surfaces for Osseointegration: An Advanced Investigation. *Appl. Surf. Sci.*, **599**, 154023 (2022).

[21] Akdoğan, E.; Şirin, H. T.; Öztatlı, H.; Kılıçarslan, B.; Bayram, C.; Garipcan, B. Adsorption Behavior of Serum Proteins on Anodized Titanium Is Driven by Surface Nanomorphology. *Biointerphases*, **18**, 061001 (2023).

[22] Nonckreman, C. J.; Fleith, S.; Rouxhet, P. G.; Dupont-Gillain, C. C. Competitive Adsorption of Fibrinogen and Albumin and Blood Platelet Adhesion on Surfaces Modified with Nanoparticles and/or PEO. *Colloids Surf. B Biointerfaces*, **77**, 139-149 (2010).

[23] Weber, M.; Steinle, H.; Golombek, S.; Hann, L.; Schlensak, C.; Wendel, H. P.; Avci-Adali, M. Blood-Contacting Biomaterials: In Vitro Evaluation of the Hemocompatibility. *Front. Bioeng. Biotechnol.*, **6**, 99 (2018).

[24] Zhang, C.; Cheng, X.; Zhao, R.; Fu, M.; Wang, M.; Chen, Z.; Zhang, C.; Li, X. Enhanced antibiotic removal via magnetic Ni@ZIF-8 composite nanotubes: Synergistic adsorption, facile recovery and adsorption mechanism. *Sep. Purif. Technol.*, **363**, 131988 (2025).

[25] Cheng, X.; Liu, C.; Cai, Y.; Li, X.; Zhao, R.; Feng, Y.; Wang, M. Construction and Biological Evaluation of Different Nanoshell Thickness Ni@SiO_2 Nanotubes as Good Protein Separation Carriers for Bovine Hemoglobin. *Curr. Med. Chem.*, **32**, 6867-6881 (2025).

[26] Liu, C.; Dai, J.; Wang, J.; Hu, C.; Fu, M.; Wang, M.; Lin, X.; Cheng, X.; Li, X. Core-Shell Structured Nickel@Polydopamine Magnetic Composite Nanotubes for Chelator-Free Protein Removal: Self-Released Ni^{2+}-Mediated Selective Adsorption of Histidine-Rich Proteins. *Talanta*, **300**, 129143 (2026).

[27] Wu, G.; Zhang, C.; Liu, C.; Li, X.; Cai, Y.; Wang, M.; Chu, D.; Liu, L.; Tian, M.; Chen, Z. Magnetic Tubular Nickel@Silica-Graphene Nanocomposites with High Preconcentration Capacity for Organothiophosphate Pesticide Removal in Environmental Water: Fabrication, Magnetic Solid-Phase Extraction, and Trace Detection. *J. Hazard. Mater.*, **457**, 131788 (2023).

[28] Mu, Z.; Zhao, H.; Zhang, W.; Ni, R.; Zhang, Z.; Shang, D.; Wang, Y.; Wei, Q.; Pan, J.; Yang, F. Construction of MOF-on-Montmorillonite Composite for Excellent Synchronous Decontamination: Oxidative Degradation Coupled with Adsorption Removal of Heavy Metal Ions. *Sep. Purif. Technol.*, **386**, 136535 (2026).

[29] Ni, R.; Opoku, K. N.; Li, X.; Gao, Y.; Wang, Y.; Yang, F. Recent Advance in Utilization of Advanced Composite Photothermal Materials for Water Disinfection: Synthesis, Mechanism, and Application. *Chin. Chem. Lett.*, **36**, 110813 (2025).

[30] Wu, X.; Liu, M.; Zhao, H.; Shang, D.; Wang, Y.; Zeng, F.; Shen, J.; Pan, J.; Liu, X.; Song, Y.; Yang, F. Constructing Confinement-Protected Co_3O_4 into Nanocarbon Shells onto Mn_2O_3 Nanorod Allows for Efficient PMS Activation and Contaminant Elimination. *Mol. Catal.*, **574**, 114888 (2025).

[31] Zhang, Y.; Zhao, H.; Zhou, J.; Wang, Y.; Pan, J.; Ang, E. H.; Yang, F. Photothermal halloysite nanotube hybrids with

CoO/carbon layers for enhanced pollutant degradation and solar-powered water purification. *Desalination*, **602**, 118630 (2025).

[32] Prakasam, H. E.; Shankar, K.; Paulose, M.; Varghese, O. K.; Grimes, C. A. A New Benchmark for TiO_2 Nanotube Array Growth by Anodization. *J. Phys. Chem. C*, **111**, 7235-7241 (2007).

[33] Watcharenwong, A.; Chanmanee, W.; Tacconi, N. R. de; Chenthamarakshan, C. R.; Kajitvichyanukul, P.; Rajeshwar, K. Self-Organized TiO_2 Nanotube Arrays by Anodization of Ti Substrate: Effect of Anodization Time, Voltage and Medium Composition on Oxide Morphology and Photoelectrochemical Response. *J. Mater. Res.*, **22**, 3186-3195 (2007).

[34] Albu, S. P.; Tsuchiya, H.; Fujimoto, S.; Schmuki, P. TiO_2 Nanotubes-Annealing Effects on Detailed Morphology and Structure. *Eur. J. Inorg. Chem.*, **2010**, 4351-4356 (2010).

[35] Yang, L.; Zhang, M.; Shi, S.; Lv, J.; Song, X.; He, G.; Sun, Z. Effect of Annealing Temperature on Wettability of TiO_2 Nanotube Array Films. *Nanoscale Res. Lett.*, **9**, 621 (2014).

[36] Macak, J. M.; Tsuchiya, H.; Taveira, L.; Aldabergerova, S.; Schmuki, P. Smooth Anodic TiO_2 Nanotubes. *Angew. Chem. Int. Ed. Engl.*, **44**, 7463-7465 (2005).

[37] Macak, J. M.; Aldabergerova, S.; Ghicov, A.; Schmuki, P. Smooth Anodic TiO_2 Nanotubes: Annealing and Structure. *Phys. Status Solidi A*, **203**, R67-R69 (2006).

[38] Lamberti, A.; Chiodoni, A.; Shahzad, N.; Bianco, S.; Quaglio, M.; Pirri, C. F. Ultrafast Room-Temperature Crystallization of TiO_2 Nanotubes Exploiting Water-Vapor Treatment. *Sci. Rep.*, **5**, 7808 (2015).